

A numerical study of gas focused non-Newtonian micro-jets

Rizwan Zahoor^a, Saša Bajt^{b,c}, Božidar Šarler^{a,d,*}

^a Laboratory for Fluid Dynamics and Thermodynamics, Faculty of Mechanical Engineering, University of Ljubljana, Aškerčeva 6, Ljubljana 1000, Slovenia

^b Center for Free-Electron Laser Science CFEL, Deutsches Elektronen-Synchrotron DESY, Notkestr. 85, Hamburg 22607, Germany

^c The Hamburg Centre for Ultrafast Imaging, Luruper Chaussee 149, Hamburg 22761, Germany

^d Laboratory for Simulation of Materials and Processes, Institute of Metals and Technology, Lepi pot 11, Ljubljana 1000, Slovenia

ARTICLE INFO

Keywords:

Serial crystallography
Flow-focusing
Gas dynamic virtual nozzle
Liquid jets
Multiphase flow
Fluid rheology
Non-Newtonian fluid
Power law
Shear thinning
Shear thickening

ABSTRACT

The present numerical study assesses the jet length, diameter and velocity of various non-Newtonian power-law fluids of a gas dynamic virtual nozzle. A related two-phase flow problem is formulated within the mixture framework and solved with the finite volume method and volume of fluid interface treatment in axisymmetry. The process parametric range allows the incompressible laminar flow assumption. A comprehensive jet characteristics analysis is carried out in a typical micro-nozzle configuration for a range of shear-thinning to shear-thickening fluids with power law indices $0.5 \leq n < 1.5$, gas mass flow rate of 10 mg/min and liquid volumetric flow rate of 43 $\mu\text{l}/\text{min}$, resulting in a gas Reynolds number of 130 with Reynolds and Weber numbers for a reference water jet being 90 and 10, respectively. It is observed that jets from shear-thinning fluids ($0.5 \leq n < 1.0$) tend to be thicker, longer, and slower when compared with the shear-thickening fluids ($1.0 < n \leq 1.5$). A dripping-jetting phase diagram of the nozzle is constructed by varying the power law index, gas and liquid flow rates in the range 0.9–1.1, 5–15 mg/min and 5–50 $\mu\text{l}/\text{min}$, respectively. It is observed that the area of stable jetting decreases with the increase of the power law index. The obtained novel information on the behaviour of non-Newtonian gas-focused micro-jets provides a possible new dimension for tailoring the serial crystallography sample delivery systems where the micro-jets carry dispersed crystals into an X-ray beam.

1. Introduction

Microfluidics has emerged in a wide range of applications, such as food safety (Nilghaz et al., 2021), drug screening (Sun et al., 2019), material synthesis (Günther and Jensen, 2006), and bioengineering (Finehout and Tian, 2009). Liquid jets emanating from micro nozzles are also commonly used for sample delivery in serial crystallography (SX) experiments (Grünbein and Kovacs, 2019; Weierstall, 2014; Zhao et al., 2019) at synchrotrons and X-ray Free Electron Lasers (XFELs). This development is described in recent review papers (Cheng, 2020; Hejazian et al., 2020). They can also be used as precursors to monodispersed droplet generation for microencapsulation (Lee et al., 2016) in the pharmaceutical industry. Although most of the microfluidics applications involve Newtonian fluids, a handful of applications such as microreactors (Dessimoz et al., 2008), drug delivery (Fontana et al., 2016), lab-on-a-chip (Stone et al., 2004), cell encapsulation (Navi et al., 2018), and serial femtosecond crystallography (SFX) (Weierstall, 2014), involve complex, non-Newtonian liquids. They can include varying

concentrations of polymers, surfactants, and biological/non-biological matter. The presence of non-Newtonian fluids, with a nonlinear relationship between shear stress and strain rate, essentially defines the hydrodynamic response of the microfluidic entities (Kumari and Atta, 2022; Qiu et al., 2010) differing much from the Newtonian behaviour.

Increased utilization of micro-jets in sample delivery for SFX at XFELs and SX at synchrotrons demands continuous improvements in their performance. In SFX experiments (Chapman et al., 2011), the high-intensity X-ray pulses diffract from the micro-crystals dispersed in the micro-jets. If pulses are short enough (in the femtosecond regime), the diffraction happens before the crystals are altered or destroyed, and the diffraction data can be used to obtain information on the protein structure (Neutze et al., 2000) or even time evolution in protein conformations. However, the high frequency of X-ray pulses requires replenishment of destroyed samples before the arrival of the next X-ray pulse. The required velocity depends on the XFEL operational frequency. Additionally, the weak diffraction signals from micron to submicron crystals require minimizing the background signal to gather high-quality

* Corresponding author at: Laboratory for Fluid Dynamics and Thermodynamics, Faculty of Mechanical Engineering, University of Ljubljana, Aškerčeva 6, Ljubljana 1000, Slovenia.

E-mail address: bozidar.sarler@fs.uni-lj.si (B. Šarler).

<https://doi.org/10.1016/j.ijmultiphaseflow.2023.104628>

Received 11 May 2023; Received in revised form 30 August 2023; Accepted 4 October 2023

Available online 8 October 2023

0301-9322/© 2023 The Authors. Published by Elsevier Ltd. This is an open access article under the CC BY-NC-ND license (<http://creativecommons.org/licenses/by-nc-nd/4.0/>).

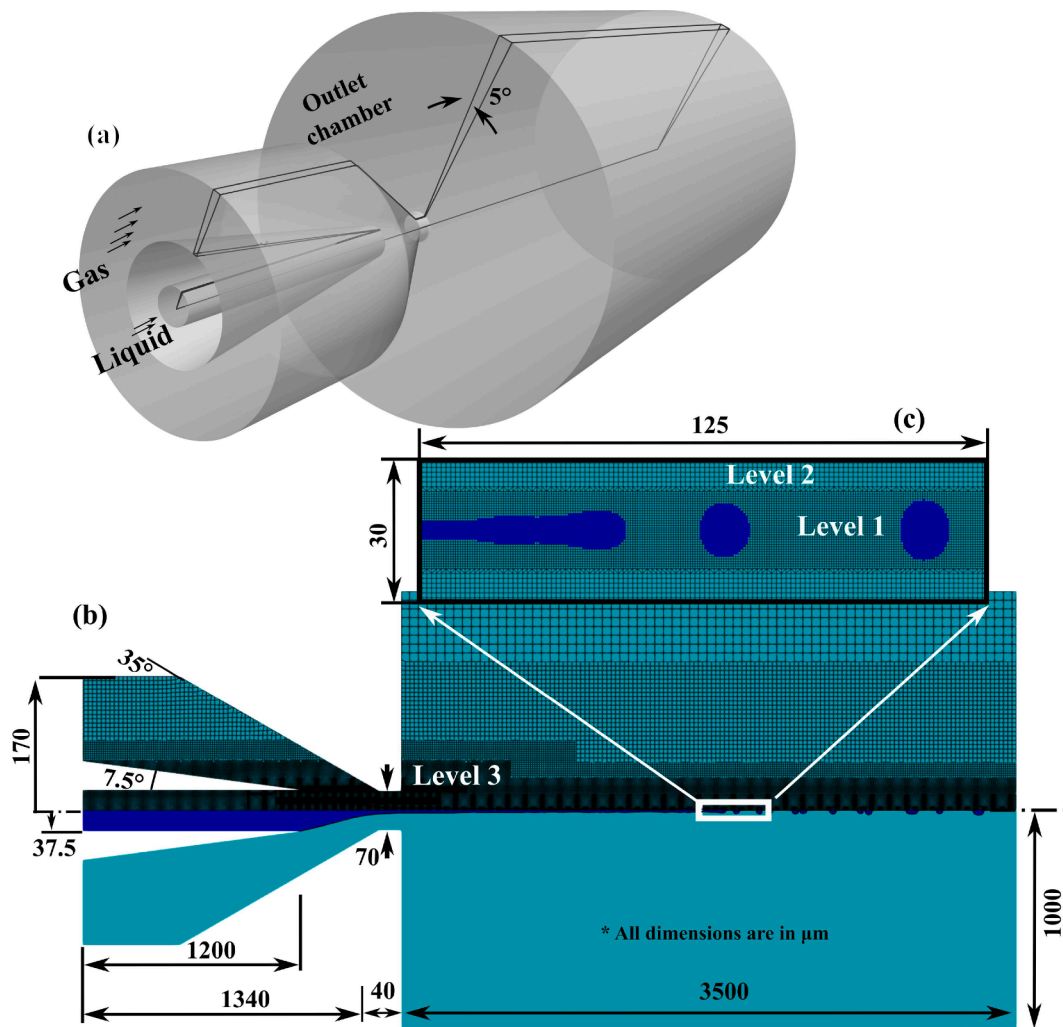


Fig. 1. Scheme of computational domain with (a) actual nozzle, (b) axisymmetric domain modelling, (c) control volume arrangement with levels 1, 2, and 3 and respective cell sizes of 0.5, 1.0 and 2.0 μm . The blue colour represents the liquid.

Table 1

An overview of boundary conditions at six boundary patches.

Patch	Velocity	Pressure	Phase fraction
Inlet liquid	$Q_l = Q_c$	$\frac{\partial p}{\partial n} = 0$	$\alpha = 1$
Inlet gas	$m'_g = m'_c$	$\frac{\partial p}{\partial n} = 0$	$\alpha = 0$
Walls	$\mathbf{v} = 0$	fixedFluxPressure ^[1]	$\frac{\partial \alpha}{\partial n} = 0$
Outlet	$\frac{\partial \mathbf{v}}{\partial n} = 0$	$p = 101325 \text{ Pa}$	$\frac{\partial \alpha}{\partial n} = 0$
Front	wedge ^[2]		
Back	wedge		

^[1] This boundary condition sets the pressure gradient to the provided value such that the flux on the boundary is specified by the velocity boundary condition.

^[2] A special boundary condition to enforce cyclic conditions between the two patches.

data. Ideally, the protein crystals should stay in their native environment (water or buffer) until they interact with X-rays with the minimum amount of liquid around them. This necessitates that the jet diameters are commensurate to the X-ray and crystals sizes ($\sim 1 \mu\text{m}$ or below). Finally, to avoid shadowing from the nozzle, the sample-beam interaction should ideally happen at least $100 \mu\text{m}$ from the nozzle outlet. Consequently, the stable jet length must be long enough to ensure

interaction at such distances.

The purpose of the present paper is to investigate the effects of the non-Newtonian shear-thinning/thickening fluid rheology on the micro-jet characteristics.

The limitation of Rayleigh jets (Rayleigh, 1879) to miniaturization leaves flow-focusing (Gañán-Calvo, 1998) as the standard choice for producing liquid jets for SFX experiments. A focusing momentum from a co-flowing sheath gas is imparted to a liquid stream issuing from a feeding capillary of a gas dynamic virtual nozzle (GDVN) (DePonte et al., 2008). GDVN's are now routinely prepared using 3D printing technology (Nelson et al., 2016).

The multiphase jet flows in GDVNs involve complicated contributions of various cohesive and disruptive forces. The complex interaction of such forces dictates the ultimate behaviour of the resulting jets and droplets. They are influenced by fluid rheology, gas type, nozzle geometry, and process parameters (Zahoor et al., 2021a; Zhang et al., 2020). Depending upon the involved fluids' rheology, the shear produced at the liquid-gas interface acts as a countering agent against the interfacial instabilities and resulting jet breakup. The speed of the co-flowing gas significantly influences the jet characteristics. Various stability analyses have been performed on the energy transfer and force balances between liquid and gas flows in incompressible (Huerre and Monkewitz, 1990; Vega et al., 2010) and compressible (Rubio et al., 2021) regimes. The jets for SFX are mostly used in a vacuum environment, making the gas compressibility effects significant (Rubio et al.,

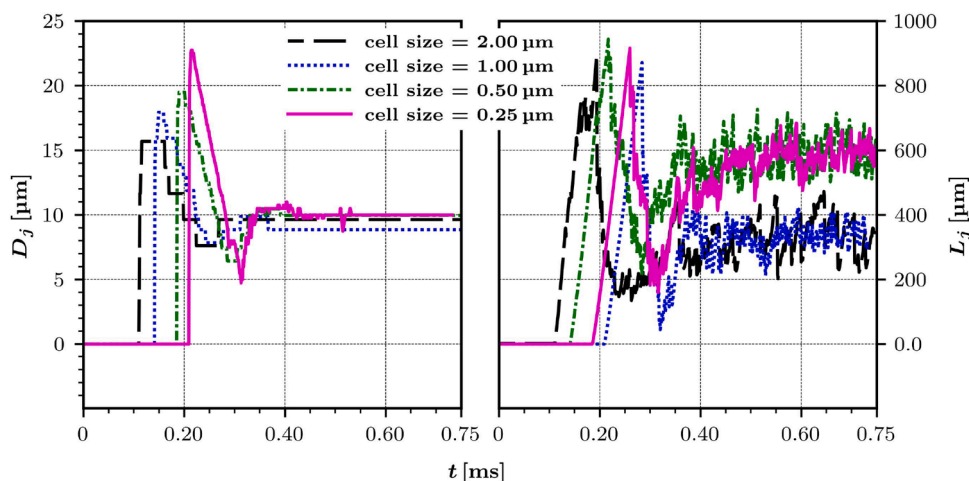


Fig. 2. Jet diameter and jet length at the nozzle outlet as a function of time and cell size for $n = 1.0$ (pure water) with gas and liquid flow rates of 10 mg/min and 43 $\mu\text{l}/\text{min}$, respectively.

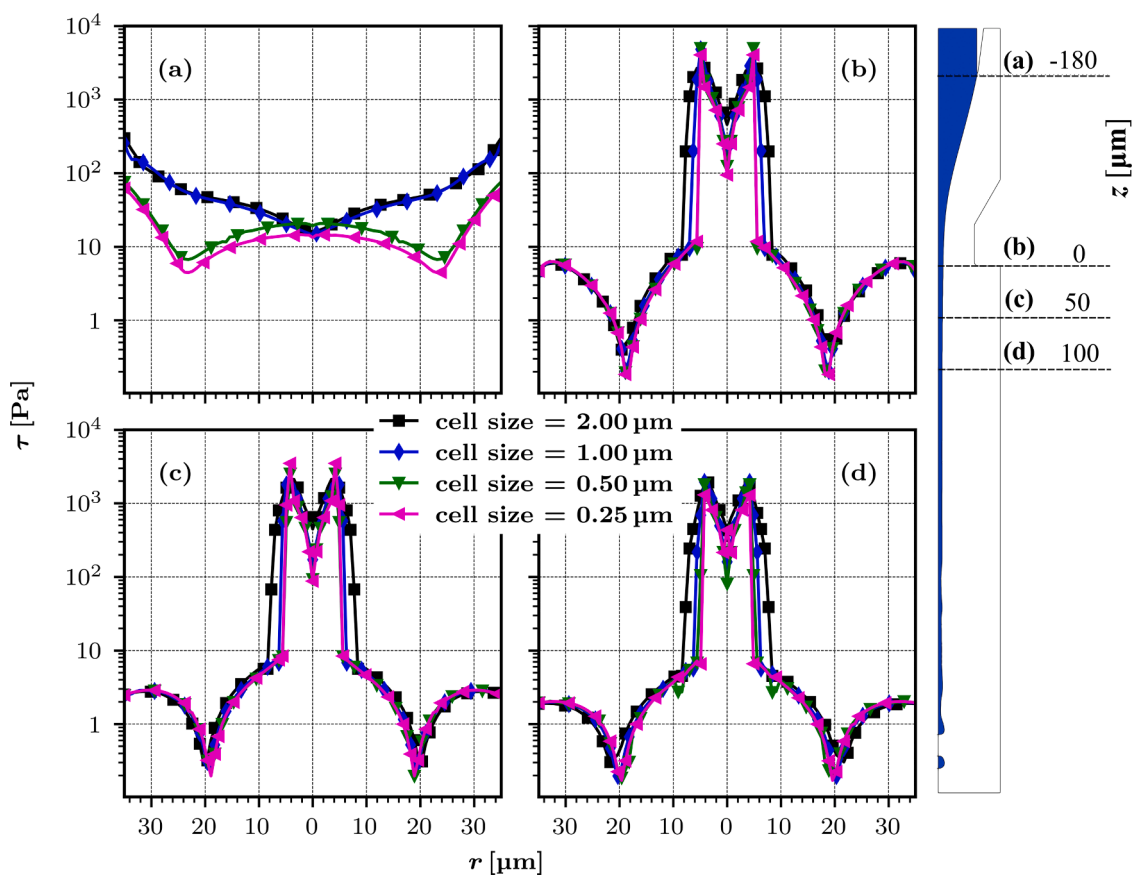


Fig. 3. Shear stress profiles of Newtonian fluid ($n = 1.0$) as a function of radius at 4 axial positions along the jet and mesh density with gas and liquid flow rates of 10 mg/min and 43 $\mu\text{l}/\text{min}$, respectively.

2021). Rubio et al. (2022b) experimentally found that introducing viscoelasticity in transonic jet focusing reduces the liquid flow rate required to produce stable jets.

The experimentally validated (Dupin et al., 2006; Herrada et al., 2008; Nazari et al., 2023; Zahoor et al., 2021b) numerical approaches have been recently successfully utilized to study the Newtonian jet breakup behaviour as a function of the process (Zahoor et al., 2018c), geometrical (Sarler et al., 2021; Zahoor et al., 2018a), and material parameters (Zahoor et al., 2020, 2018b). All these studies offer

systematic information on the complex behaviours of these multiphase flows but are limited to Newtonian fluids. The presence of crystals changes the behaviour of these jets from Newtonian to complex non-Newtonian. Additionally, in some settings, highly viscous non-Newtonian fluids (lipidic cubic phase) are extruded from feeding capillaries 10 - 50 μm in diameter to carry membrane proteins (Weierstall, 2014). In such high-viscosity fluids, co-flowing gas helps avoid curling. Although the process involving such gas-focused jets (Martiel et al., 2019) has been investigated extensively both experimentally

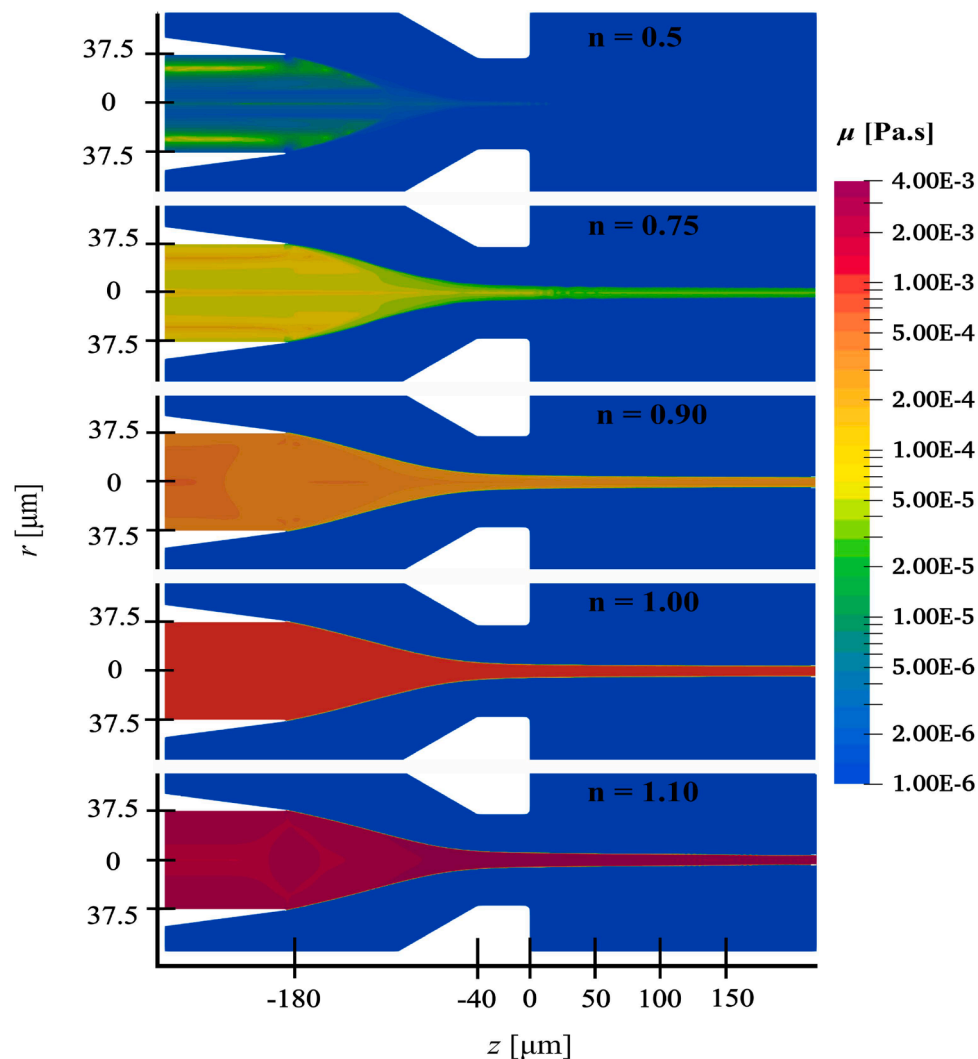


Fig. 4. Viscosity distribution in the liquid micro-jet with gas and liquid flow rates of 10 mg/min and 43 $\mu\text{l}/\text{min}$, respectively as a function of different power-law index (from top to bottom: $n = 0.5, 0.75, 0.90, 1.0,$ and 1.10).

(Beyerlein et al., 2015; DePonte et al., 2008; Echelmeier et al., 2019; Knoška et al., 2020; Oberthuer et al., 2017; Wiedorn et al., 2018) and numerically (Belšak et al., 2021; Herrada et al., 2008; Šarler et al., 2021; Zahoor et al., 2021b, 2018c, 2018a), only a few included non-Newtonian behaviours (Aliseda et al., 2008; Ertl and Weigand, 2016; Hejazian et al., 2020; Li et al., 2013; Negri et al., 2013; Ponce-Torres et al., 2016). For example, Aliseda et al. (2008) studied the atomization of non-Newtonian liquids by coaxial gas jets in co-flow atomizers used in tablet coating in the pharmaceutical industry, both theoretically and experimentally, while Ertl and Weigand (2016) performed direct numerical simulations to investigate the primary breakup phenomena of shear-thinning liquid when issued in a stagnant air environment. Ponce-Torres et al. (2016) considered the gas focusing of viscoelastic capillary jets in their experiments.

Most studies involving non-Newtonian fluids consider liquid-liquid (Derzsi et al., 2013; Edmond et al., 2006; Rostami and Morini, 2019) multiphase flows in microfluidic appliances. Rare experimental studies focused on gas focusing of viscoelastic fluids (Ponce-Torres et al., 2016) and ultrafine fibre solution blow spinning (Hofmann et al., 2018). These studies were mainly experimental and utilized plate-orifice nozzles while considering the viscoelastic behaviour of focused fluids. The numerical investigations (Shi and Tang, 2015; Sontti and Atta, 2017) reported a strong influence of the jet and droplet formation from the rheological properties of the operating fluids, in addition to surface

tension and flow rate. Additionally, numerical investigations involving non-Newtonian fluid behaviour included droplet formation in T-junction microchannel (Kumari and Atta, 2022) and droplet formation from power-law fluids in liquid-liquid flow-focusing device (Chen et al., 2020). A more comprehensive understanding of the physics of the gas-focused jet from converging GDVN involving a range of Newtonian to non-Newtonian fluids (shear-thinning/thickening) (Bergmann et al., 2017) is needed.

The inclusion of non-Newtonian rheological behaviour of focused liquid in the present paper is aimed to expand the knowledge base around previous parametric studies involving gas-focusing and the influence of external excitations (Cruz-Mazo et al., 2019; Zupan et al., 2023).

2. Model formulation and solution procedure

2.1. GDVN geometry

The problem involves a two-phase gas-liquid flow in a cylindrically symmetric GDVN, as shown in Fig. 1. Similar GDVN geometry has been discussed extensively (Zahoor et al., 2018a). The GDVN consists of an inner liquid-feeding capillary and an outer converging gas flow capillary. In the experimental setting (Zahoor et al., 2021b), the liquid and gas flow is ensured by supply lines from flow controllers.

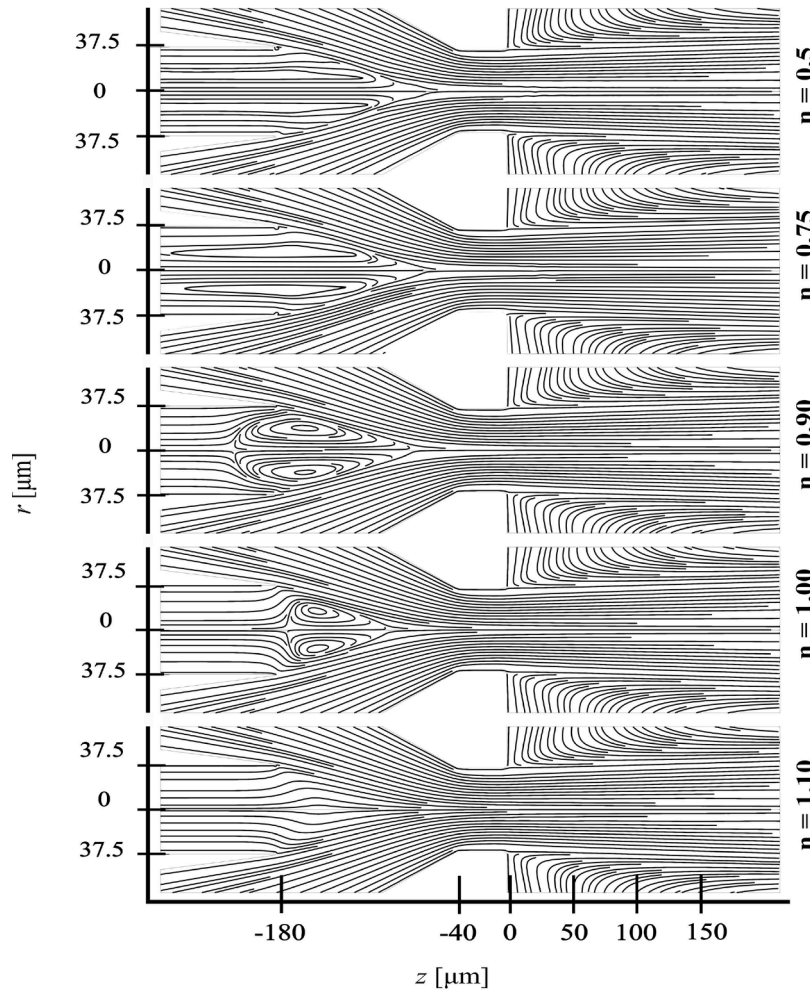


Fig. 5. The streamlines near the liquid meniscus for gas and liquid flow rates of 10 mg/min and 43 μ l/min, respectively as a function of the power-law index (from top to bottom: $n = 0.5, 0.75, 0.90, 1.0,$ and 1.10).

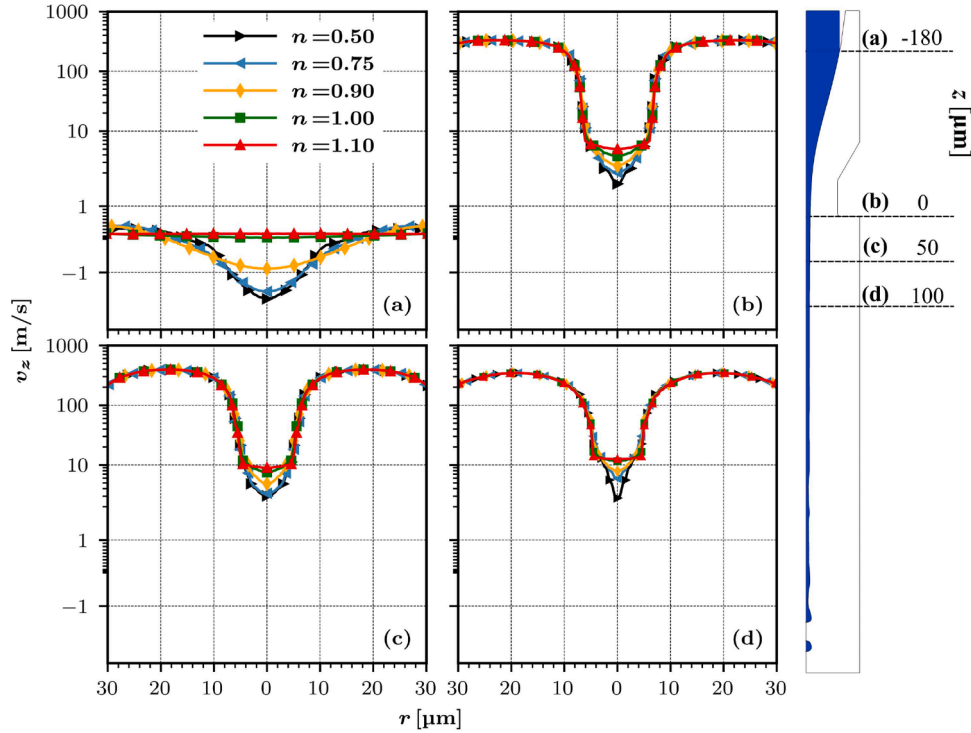


Fig. 6. The axial component of velocity (logarithmic scale) for gas and liquid flow rates of 10 mg/min and 43 $\mu\text{l}/\text{min}$, respectively as a function of the radius at four axial positions for five different power-law indexes.

2.2. Governing equations

The numerical model consists of a mixture formulated mass and momentum conservation equations of an incompressible and immiscible gas-liquid two-phase flow. The axisymmetry of the numerical model provides a reasonably good physical insight into the jet before the primary breakup. It is, however, not applicable for modelling the whipping instabilities (Blanco-Trejo et al., 2020) and secondary jet breakup. Both are out of scope in the present study since the primary interest is in operating parameters typically used in SFX to reach stable jetting. That is why the extensive computational resources used in 3D modelling (Herrada et al., 2008; Vega et al., 2010; Belšak et al., 2021; Zahoor et al., 2021b) for assessing the differences between the non-Newtonian and Newtonian jet behaviour, are not needed.

The governing mass and momentum conservation equations are as follows:

$$\nabla \cdot \mathbf{v} = 0, \quad (1)$$

$$\frac{\partial}{\partial t}(\rho \mathbf{v}) + \nabla \cdot (\rho \mathbf{v} \mathbf{v}) = -\nabla p + \nabla \cdot [2\mu(\nabla \mathbf{v})_{sym}] + \mathbf{f}_\sigma, \quad (2)$$

where \mathbf{v} represents mixture velocity, p pressure, μ kinematic viscosity, ρ density, $(\nabla \mathbf{v})_{sym} = 0.5[(\nabla \mathbf{v}) + (\nabla \mathbf{v})^T]$ symmetric part of the velocity deformation tensor, and \mathbf{f}_σ the body force due to the surface tension.

To describe the presence of (gas/liquid) phases at a given point $P(\mathbf{x}, t)$ with spatial position \mathbf{x} and time instance t , a phase function $\alpha(\mathbf{x}, t)$ is introduced such that:

$$\alpha(\mathbf{x}, t) = \begin{cases} 1 & P(\mathbf{x}, t) \in \text{liquid} \\ 0 & P(\mathbf{x}, t) \in \text{gas} \end{cases}. \quad (3)$$

In the absence of phase change, the interface advection equation is represented as:

$$\frac{\partial}{\partial t} \alpha + \mathbf{v} \cdot \nabla \alpha = 0. \quad (4)$$

The material properties of the flow field (1) and (2) are provided by volume averaging:

$$\rho = \rho_l \alpha + \rho_g (1 - \alpha) \quad (5)$$

$$\mu = \mu_l \alpha + \mu_g (1 - \alpha) \quad (6)$$

$$\mathbf{v} = [\mathbf{v}_l \rho_l \alpha + \mathbf{v}_g \rho_g (1 - \alpha)] / \rho \quad (7)$$

The volumetric representation of the surface tension force is $\mathbf{f}_\sigma = \sigma \kappa \nabla \alpha$ with σ denoting the surface tension and κ the interface curvature. The continuum surface force (Brackbill et al., 1992) model is used for estimating the interface curvature $\kappa(\alpha) = -\nabla \cdot \hat{\mathbf{n}}$, with $\hat{\mathbf{n}} = \nabla \alpha / |\nabla \alpha|$ being unit interface normal pointing from the gas to the liquid.

The compressible formulation of the subject problem has been extensively discussed in (Zahoor et al., 2018c).

There are various models available to describe the non-Newtonian fluid rheology. Amongst them are Byron and Carreau (1968), Carreau (1972), Cross (1965), Casson (1959), and the power-law Reiner (1926) model, to name a few. We assume the power-law type of non-Newtonian behaviour of the focused liquid with viscosity calculated by

$$\mu_l = K |\dot{\gamma}|^{n-1}; |\dot{\gamma}| = 2\sqrt{(\nabla \mathbf{v})_{sym} : (\nabla \mathbf{v})_{sym}}, \quad (8)$$

with K representing the consistency index and n being the power-law index. The power-law fluids are categorized into shear-thinning ($n < 1$), Newtonian ($n = 1$), and shear-thickening ($n > 1$) fluids.

The Bond number ($\text{Bo} = \Delta \rho g L^2 / \sigma$) representing the relative importance of the gravitational to surface tension force of the problem under consideration ($\Delta \rho = \rho_l - \rho_g = 998 - 0.164 = 999.83 \text{ kgm}^{-3}$, $L = 35 \mu\text{m}$, $g = 9.8 \text{ ms}^{-2}$, and $\sigma = 0.072 \text{ Nm}^{-1}$) is very small (1.5×10^{-4}), thus indicating that the gravitational forces can be neglected.

The numerical solution of Eqs. (1)-(2) is based on the finite volume method (FVM) discretization (Ferziger and Perić, 2002; Moukalled et al., 2016; Versteeg and Malalasekera, 2007), where the gas-liquid interfaces are defined by the volume of fluid (VOF) model (Hirt and

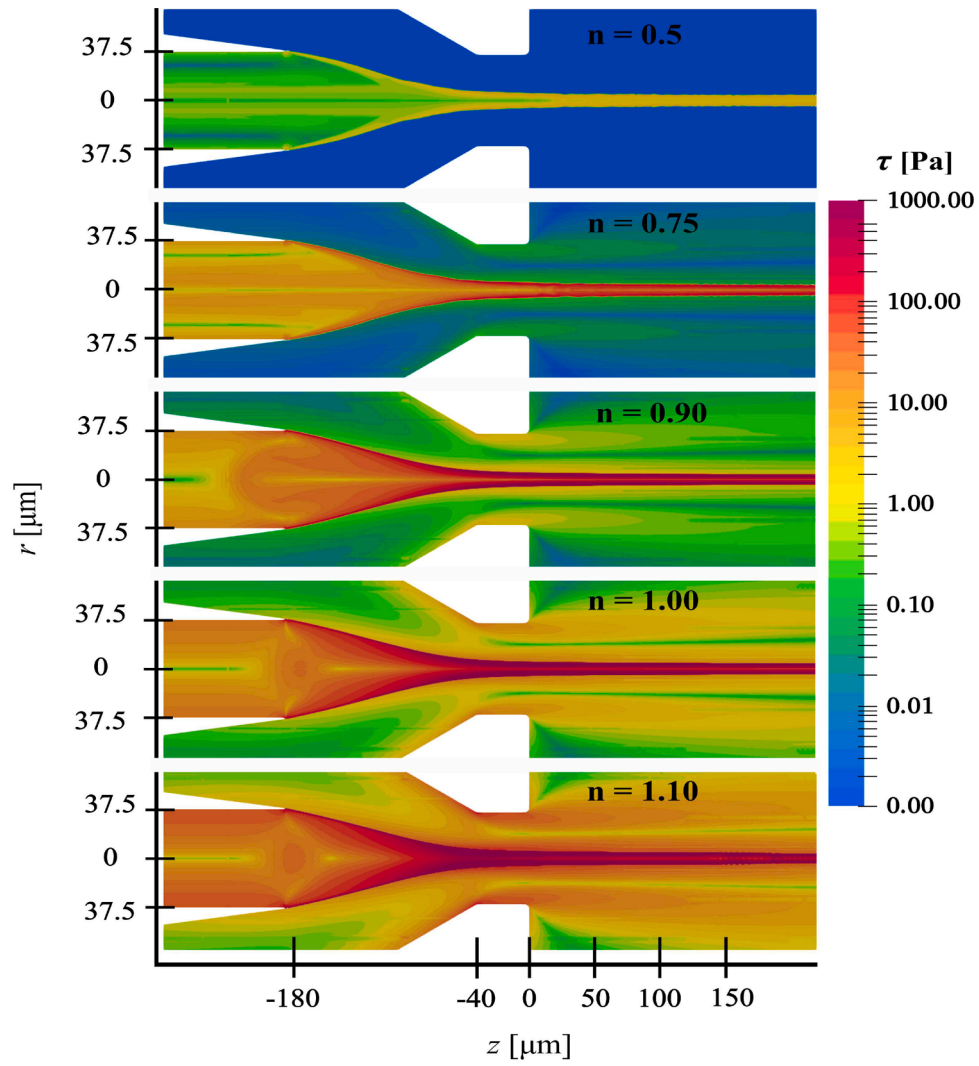


Fig. 7. Shear stress (force in the z -direction and surface in the r -direction) distribution in the liquid micro-jet with gas and liquid flow rates of 10 mg/min and 43 $\mu\text{l}/\text{min}$, respectively as a function of different power-law index (from top to bottom: $n = 0.5, 0.75, 0.90, 1.0,$ and 1.10).

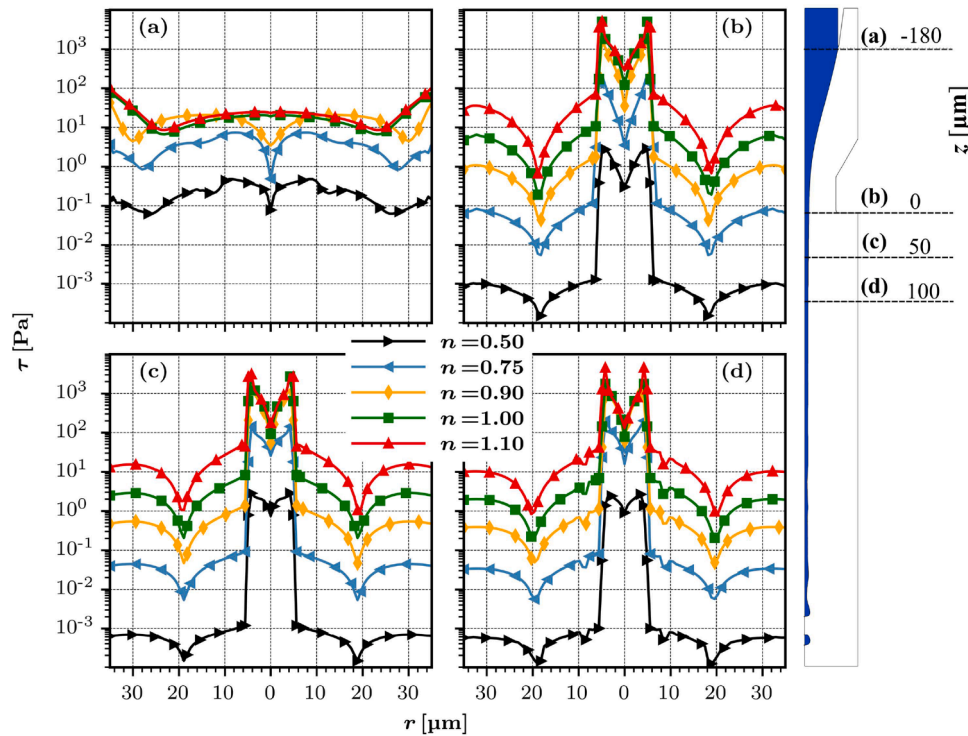


Fig. 8. Shear stress (force in z -direction, surface in r -direction) as a function of the radius at four axial positions for five different power-law indices.

Nichols, 1981). Numerical simulations are performed with OpenFOAM (Greenshields, 2022) package. The standard algebraic formulation of VOF is susceptible to interface smearing issues, which is countered by an interface compression approach (Weller, 2008). The numerical solution of axisymmetric problems with OpenFOAM requires modelling of the domain in the shape of a 5° wedge, as represented in Fig. 1-a. The bottom plane of the wedge is collapsed to the symmetry axis. The nozzle domain is discretized into $\sim 150\,000$ hexa-dominant finite volumes (Fig. 1-b). The maximum refinement is ensured in the region of interest (gas-liquid interface) with a minimum cell size of $0.5\ \mu\text{m}$ (Fig. 1-c). The cell sizes grow away from the liquid jet to a maximum of $16\ \mu\text{m}$. A scheme of the spatial distribution of control volumes over the computational domain is represented in Fig. 1-b.

The outlet domain size with the length $l = 3500\ \mu\text{m}$, and radius $h = 1000\ \mu\text{m}$, and the minimum cell size of $0.5\ \mu\text{m}$ is based on the previously reported mesh independence study for a similar nozzle and numerical model (Zahoor et al., 2018c). The boundary of the discretized numerical domain is grouped into six distinct boundary condition types. They are defined in Table 1.

A minimum of 2nd order accurate schemes is used in the solution procedure. The derivative terms are calculated using Gaussian finite-volume integration (LeVeque, 2002). A 2nd order accurate *vanLeer* Total Variation Diminishing (TVD) scheme (van Leer, 1979) is used for convective terms. Interpolation of variables from cell to face is obtained by a TVD scheme *limitedLinearV*. The transient terms are treated with *Crank-Nicolson* 2nd order accurate transient scheme. It utilizes a blending coefficient ϕ to provide blending between two schemes (0: Euler, 1: Crank-Nicolson). A value of $\phi = 0.9$ was utilized as it provides a good compromise between accuracy and robustness. For pressure-velocity coupling PIMPLE algorithm is utilized, a blend of SIMPLE and PISO algorithms. The time step is adapted based on the Courant number (Courant et al., 1967) $Co = (|v|\Delta t/\Delta x) \leq 0.30$. A detailed documentation about the implementation and guidelines for using described numerical schemes is given in (Moukalled et al., 2016).

Helium gas of constant density $\rho = 0.164\ \text{kgm}^{-3}$ and constant viscosity $\mu = 1.96 \times 10^{-5}\ \text{Pa}\cdot\text{s}$ was assumed as the focusing gas. The vis-

cosity of the focused liquid ranged from Newtonian to shear-thinning and shear-thickening. They were assumed such that the values of power-law index n were changed around water ($n = 1$) for shear-thinning $0.5 \leq n < 1$ and shear-thickening $1.5 \geq n > 1$. The consistency index ($K = 0.001\ \text{Pa}\cdot\text{s}$), density ($\rho = 1000\ \text{kgm}^{-3}$), and surface tension ($\sigma = 0.072\ \text{Nm}^{-1}$) were kept constant.

The numerical simulations were performed up to $10^{-3}\ \text{s}$. Each required $\sim 150\ \text{h}$ of computational time on 64 Intel (R) Xeon (R) processors. The resulting output data was analysed with ParaView (Ahrens et al., 2005) and Matplotlib (Hunter, 2007) to provide the jet stability, shape, velocities, viscosities, and shear stresses etc.

3. Results

The influence of the non-Newtonian behaviour of the jet was performed for the range of power-law index $n = 0.5\text{--}1.5$ at the fixed gas and liquid flow rates of $10\ \text{mg}/\text{min}$ and $43\ \mu\text{l}/\text{min}$. The choice of such operating flow rates provides a long and stable jet for a reference Newtonian water ($n = 1.0$) jet. This enables the sensitivity studies of the changes in the jet characteristics, i.e., length (L_j), diameters (D_j), and velocities (v_j) as a function of fluid rheology around the reference case. A jetting-dripping phase diagram was constructed for the range of power law, gas and liquid flow rates $0.9\text{--}1.1$, $5\text{--}15\ \text{mg}/\text{min}$ and $5\text{--}50\ \mu\text{l}/\text{min}$, respectively, to determine the mutual influence of the flow rates and non-Newtonian behaviour.

The mesh-independent numerical results for gas and liquid flow rates of $10\ \text{mg}/\text{min}$ and $43\ \mu\text{l}/\text{min}$, respectively, are ensured by conducting a related convergence study on Newtonian fluid ($n = 1.0$). Jet stability, shape, and resulting shear stresses in the vicinity of the jet are analysed as a function of control volume sizes. It is seen in Fig. 2 that the jet diameters and lengths reasonably converge for control volume sizes of $0.5\ \mu\text{m}$ and $0.25\ \mu\text{m}$. Additionally, the shear stresses generated at the gas-liquid interfaces are investigated. The shear stress profiles (force in the direction of z -coordinate and surface in the direction of r -coordinate) at 4 axial positions along the radial direction of the jet are analysed in Fig. 3. It is thus obvious that the choice of spatial discretization with 0.5

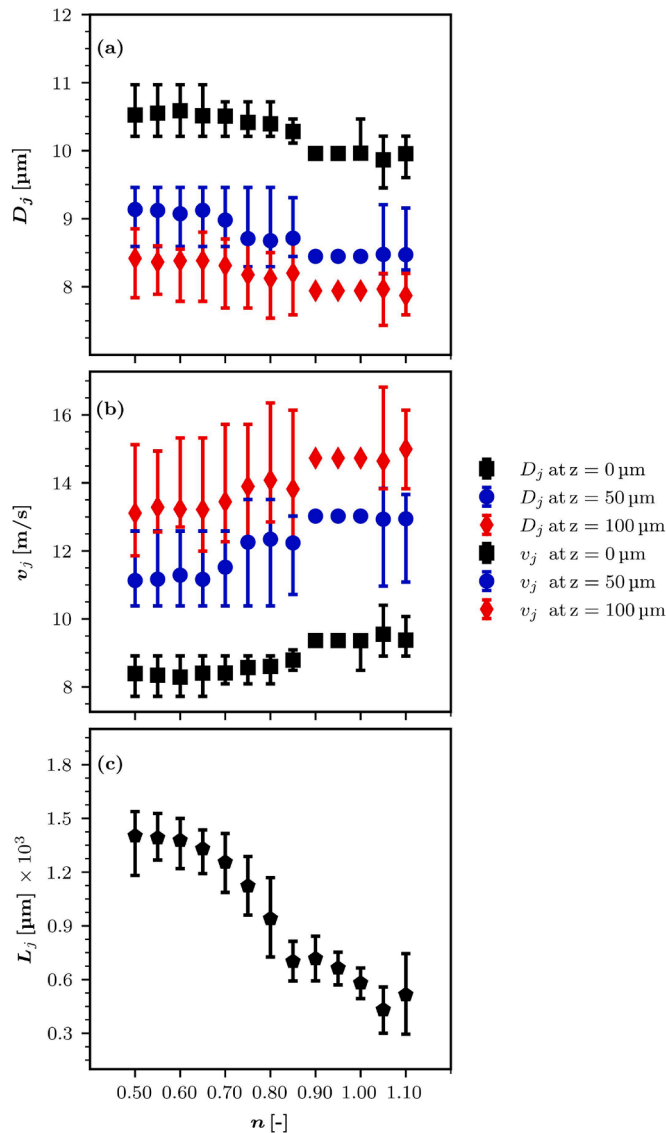


Fig. 9. Average jet (a) diameters at $z = 0, 50,$ and $100 \mu\text{m}$, (b) velocities at $z = 0, 50,$ and $100 \mu\text{m}$, and (c) length until the detachment of first droplet for gas and liquid flow rates of 10 mg/min and $43 \mu\text{l/min}$, respectively. The error bars include the maximum and minimum values, averaged over the last 0.1 ms of simulation.

μm cell size is sufficient to characterize the jet performance.

The related non-dimensional numbers involved in jet focusing, referred to the Newtonian fluid are the Reynolds number $\text{Re}_j = \rho_l Q_l / \pi R_j \mu_l = 90$ and Weber number $\text{We}_j = \rho_l Q_l^2 / \pi^2 R_j^3 \sigma = 10$.

The liquid viscosity of the jet as a function of the power-law index is provided in Fig. 4. The viscosity in the shear-thinning fluids ($n < 1.0$) decreases with the strain rate in contrast to the shear-thickening fluids ($n > 1.0$), where it increases. The decrease/increase in viscosity as a function of shear rate tends to influence the amount of shear generated at the gas-liquid interface. The shear force, along with the inertial and surface tension forces, are major driving agents in jet-focusing processes (Herrada et al., 2008). Thus, a change in any of these forces can influence the intricate balance between them, causing an overall impact on the jet's stability, shape, and velocity.

The shear stress on the liquid due to co-flowing gas causes a pulling effect on the liquid meniscus, triggering a pressure build-up in the tip of the meniscus. Such pressure built-up tends to relieve upstream in liquid feeding capillary and downstream in the chamber. The shear-thinning

fluids ($n < 1$) can be easily pushed back, causing a strong recirculation in the liquid capillary. Such cause and effect are evident in Fig. 5, where large recirculation structures appear for $n = 0.5$. When the fluid becomes increasingly shear-thickening, the size of the recirculation region decreases and vanishes for $n > 1.1$. This is happening because the effectively higher viscosity fluids are more resistant towards backward flows and relieve the momentum build-up by issuing a jet in the downstream direction.

For a given nozzle geometry, fixed operating condition (10 mg/min) and material properties of the gas, the velocity away from the gas-liquid interface does not show any significant changes, as shown in Fig. 6. Considerable changes can be seen near the interface and inside the jet due to the changes in liquid rheology. In shear-thinning fluids ($n < 1.0$) the jet's viscosity drops near the liquid-gas interface and the transfer of momentum to the core is thus reduced. The shear-thinning fluids are thus substantially slower in the core of the jet than the Newtonian fluid ($n > 1.0$). It is also observed that the velocity profiles in Fig. 6, for shear-thinning liquids ($n = 0.5, 0.90,$ and 0.75) have negative velocity peaks near the symmetry line in liquid meniscus region (Fig. 6-a). On the other hand, with the shear thickening fluids ($n > 1.0$), the jet assumes a plug type flow, i.e., moving with an almost constant speed over its cross-section. It is also apparent that the recirculation (negative axial velocities in Fig. 6-a) in the jet meniscus disappears as soon as the rheological behaviour changes from thinning to thickening ($n > 1.0$).

The direct consequence of changes in the viscosity of jetting liquid is the amount of shear stress present at the interface. Such shear is produced due to the relative velocities of the liquid and gas. It is obvious from Figs. 7 and 8 that the shear induced by the co-flowing gas is smaller in shear-thinning fluids compared to thickening fluids. Since the gas slows down in the downstream direction in the outlet chamber, the shear stresses also decrease. The maximum shear stress is present near the gas-liquid interface of the jet, while it decreases towards the centre of the jet. The shear force at the gas-liquid interface compresses, stabilizes, and accelerates the jets.

The diameter of the liquid jet (the radial position where $\alpha = 0.5$) at a certain axial position z is calculated by integrating the liquid fraction as:

$$D_j(t) = 2 \sqrt{2 \int_0^{r_{\max}(z)} \alpha(r, z, t) r dr}, \quad (9)$$

where $r_{\max}(z)$ is the maximum radial distance to the domain's boundary at the position z .

After passing the initial transient period, the jet attains a stable shape. At such conditions, the jet diameter is averaged over a reasonable time interval $\Delta t = 0.1 \text{ ms}$ as:

$$D_j(t) = \frac{1}{\Delta t} \int_{t_i}^{t_i + \Delta t} D_j(t) dt. \quad (10)$$

In present simulations, for a single gas and liquid flow rate of 10 mg/min and $43 \mu\text{l/min}$, respectively, the averaging is calculated over the last 100 output records, with each time record at an interval of $1 \mu\text{s}$ (i.e., a total of 0.1 ms averaging time). Average values obtained from Eq. (10) are represented along with minimum and maximum values as a function of the power-law index in Fig. 9. It is evident that the jet diameter decreases when moving from the shear-thinning to shear-thickening fluids. There is no considerable change in average jet diameter and velocities when n is increased from 0.9 to 1.10 . This is attributed to the fact that there are no substantial changes in shear force between the interval $0.9 \leq n \leq 1.10$ (seen in Fig. 8). The jet diameter stays stable over the averaging interval thus the minimum, average and maximum values are the same. The jet diameter decreases considerably from the nozzle outlet to a distance of $50 \mu\text{m}$, followed by a further slight decrease to a length of $100 \mu\text{m}$. This is due to the combined effect of the highest focusing momentum from co-flowing gas and variations in liquid viscosities due to

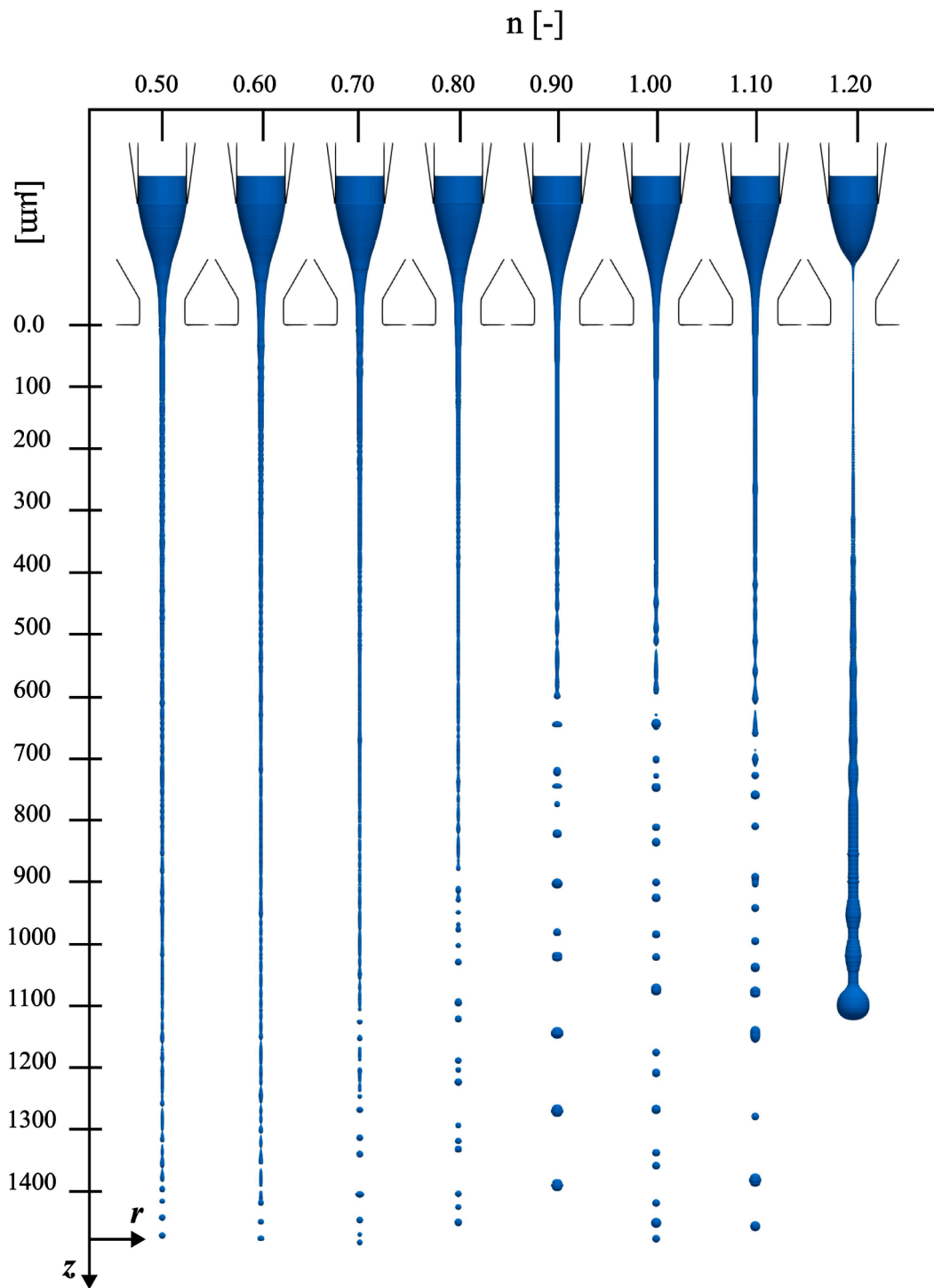


Fig. 10. Snapshot representation of liquid columns as a function of the power-law index (n).

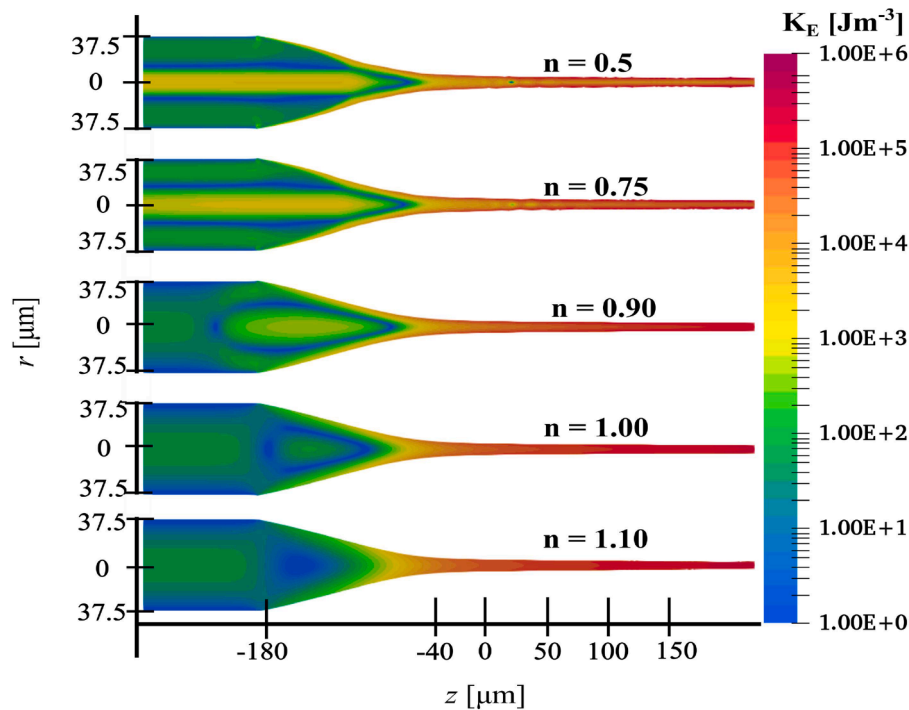


Fig. 11. The distribution of volume averaged kinetic energy of the jet for the gas and liquid flow rates of 10 mg/min and 43 $\mu\text{l}/\text{min}$, respectively as a function of the power-law index (from top to bottom: $n = 0.5$, 0.75, 0.90, 1.0, and 1.10).

strain rate. The gas momentum is highest in the region where it emanates in the outlet chamber, with a considerable compression of the liquid jet up to 50 μm length. From 50 μm to 100 μm , the change in the gas velocity is negligible and has almost no influence on the jet diameter.

Similarly, Fig. 9-b shows the increase in average velocity of the resulting jets with the transition from shear-thinning to shear-thickening fluids. The reason for slow velocities of the jet is the presence of large energy sinks in the meniscus of the jet. The momentum from the co-flowing gas is not efficiently transferred to the liquid emanating from the feeding capillary, resulting in thicker and slower jets. As these energy sinks decrease for shear-thickening fluids, the focusing gas can efficiently transfer momentum to produce thinner and faster jets.

The liquid jet after issuing from the feeding capillary requires a considerable exchange of kinetic energy from the gas to stabilize and gain acceleration. In addition to the energy consumed by the recirculation sinks, the energy consumption by the jets is scaled as $\approx \sigma/D_j$ (Gañán-Calvo, 1998). Thus, the thinner jets require more energy from the gas to keep the sophisticated balance with surface tension forces. So, with the constant operating (gas and liquid flow rates of 10 mg/min and 43 $\mu\text{l}/\text{min}$, respectively) and geometric properties, surface tension force becomes a dominant force in thinner jets, causing them to start pinching into droplets earlier and resulting in shorter jets. The same trend is also seen in Figs. 9 and 10. These results agree with the previously reported study (Zahoor et al., 2020) on the surface tension influence on the jet length.

An interesting aspect arises from the jet shape in Fig. 9, showing an increase in jet stability and length for shear-thinning fluids, although having larger recirculating structures (Fig. 5), and stretching further back in the liquid-feeding capillary. Herrada et al. (2008) have extensively discussed the recirculation cells in the liquid meniscus, their development, and their consequence on jet stability. They observed that such recirculation structures considerably influence jet stabilities, but their investigations were limited to Newtonian constant viscosity liquids. The decreasing viscosity with increasing shear rate in shear-thinning liquids demands less energy from co-flowing sheath gas for a stable jet. With lower viscosity ($n < 1.0$) at the surface than in the

core, the jets accelerate more at the surface, making it easier for the surface instabilities to be convected downstream, resulting in longer and more stable jets.

At 10 mg/min and 43 $\mu\text{l}/\text{min}$ gas and liquid flow rates, the power-law index increases above 1.1, which makes the jet unstable. The instability starts from the nozzle outlet and a compact thread breaks at the meniscus. This process, which repeats in time, is called spurting. It occurs due to the high liquid viscosity, preventing the aerodynamic forces from the co-flowing gas to shape the jet. The attached liquid drop collects at the tip of the liquid thread as it travels downstream (Fig. 10). The co-flowing gas there does not have enough tangential stress to form and sustain the jet.

To further investigate the influence of varying liquid viscosities on jet acceleration, the volume-specific kinetic energy of the liquid ($K_E = 0.5\alpha\rho_l|v_l|^2$) as a function of liquid rheology is analysed in Fig. 11. The kinetic energy plots explain the effectiveness of the momentum transfer from the co-flowing gas to liquid. With the constant gas flow rate, the velocity available from the co-flowing gas is constant. The effectiveness of the momentum transfer is correlated to the relative velocities of gas and liquid, which in turn depend upon the gas and liquid viscosities. In the case of shear-thickening fluids, the higher liquid-gas viscosity ratios produce a higher interface shear, resulting in efficient momentum transfer to the jet and, consequently, faster jets.

The effect of the liquid viscosity on the jet formation and later stabilization is summarized in Fig. 12 where the temporal evolution of the process is demonstrated. With an increase in n , the spurting ligaments increase in length while their frequency decreases. This results in the process moving further away towards the full dripping mode (for higher n values). The time evolution of the jet from Newtonian ($n = 1.0$) to shear-thickening ($n > 1.0$) values depicts that as the liquid rheological properties move towards shear-thickening, the jet becomes more viscous, requiring more influence from the co-flowing gas to remain stable.

For a given gas flow rate, a minimum liquid flow rate occurs (Vega et al., 2010), below which the stable jetting ceases to occur. This is caused by the disturbance in intricate force balance driving the jetting

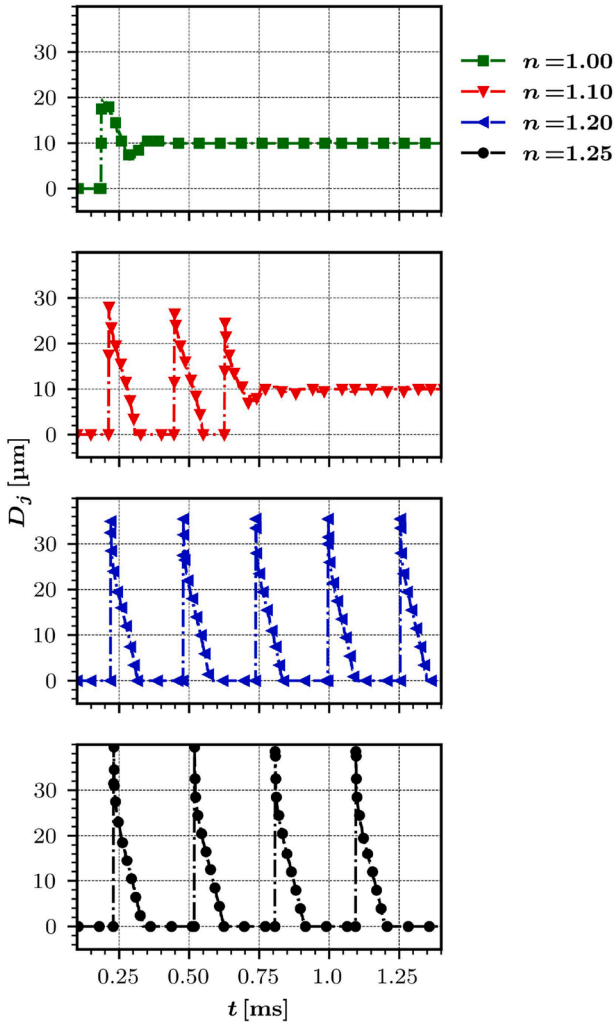


Fig. 12. Diameter of the jet at $z = 0 \mu\text{m}$ as a function of time for Newtonian and shear thickening fluids at the outlet of GDVN.

phenomenon. For lower gas flow rates, when the liquid is drawn from the feeding capillary, it tends to overshoot the equilibrium length due to liquid inertia. Without sufficient focusing force from co-flowing gas, the instabilities travel upstream, causing the jet to pinch at the meniscus tip. The meniscus oscillates in such repetitive spurting mode, and a stable jet is not achieved, as shown in Fig. 12.

The stability limits of the considered flow-focusing configuration (see Fig. 13) show that for shear-thickening liquids, the jet stability is

limited in the upper right corner between gas flow rates of 10 and 15 mg/min with liquid flow rates above 45 and 40 $\mu\text{L}/\text{min}$, respectively. The stability border decreases with the Newtonian and shear-thinning fluids, enlarging the stable jet area. The increased gas flow required for a stable jet, shown in Fig. 13-(c), confirms that a higher focusing momentum from the co-flowing gas is necessary for a stable viscous shear-thickening jet.

By increasing the gas flow rate, the compressibility might become important. Thus, we compared the incompressible numerical model with the compressible one (Zahoor et al., 2018c) to assess the possible differences. The liquid jet shapes and resulting viscosity changes are presented in Figs. 14 and 15. The compressible and incompressible results agree well, demonstrating that the computationally efficient incompressible numerical model is adequate for the considered parametric range.

Finally, we analyse three different realistic fluids: Newtonian ethyl alcohol, shear-thinning carboxymethyl cellulose (CMC) solution and shear-thickening granular solution. We used the following parameters ($n = 1.0$, $K = 0.0016 \text{ Pa}\cdot\text{s}$, $\rho = 800 \text{ kgm}^{-3}$, $\sigma = 0.024 \text{ Nm}^{-1}$) for Newtonian ethyl alcohol (Dean, 1990), ($n = 0.20$, $K = 11.9 \text{ Pa}\cdot\text{s}$, $\rho = 1000 \text{ kgm}^{-3}$, $\sigma = 0.038 \text{ Nm}^{-1}$) for shear-thinning carboxymethyl cellulose (CMC) solution (Lin and Ko, 1995), and ($n = 1.4$, $K = 0.0043 \text{ Pa}\cdot\text{s}$, $\rho = 1000 \text{ kgm}^{-3}$, $\sigma = 0.072 \text{ Nm}^{-1}$) for shear-thickening granular solution (Baek and Kim, 2011). Shear-thinning and Newtonian fluids provide long and stable jet, while there is pull-out (Rubio et al., 2022a) or spurting instability of the jet for shear-thickening granular solution, as seen in Fig. 16. For shear-thickening granular solution, initially a longer and thicker liquid ligament comes out from the nozzle outlet (see Fig. 17). The jet bulges to the extent that a free surface pinches due to pull-out instability, a consequence of normal stress imbalance between the inlet and outlet of the liquid meniscus (Rubio et al., 2022a). For a short time, the breakup produces a thinner liquid column (see Figs. 16 and 17) until a new thicker liquid volume bulges out. The process continues, where each initially thick ligament is followed by a thinner jet.

4. Conclusions

A comprehensive numerical investigation of the behaviour of gas-focused non-Newtonian shear-thinning and shear-thickening power-law fluids is performed. The numerical solution is obtained within the FVM-VOF framework. The power-law index is systematically varied within $0.5 \leq n \leq 1.5$, keeping the gas and liquid flow rates constant inside a given GDVN. It is observed that fluid rheology largely influences the shear forces generated at the gas-liquid interface. The resulting influence is quantified in terms of the jet stability, shape, and flow characteristics. Decreased liquid viscosity in shear-thinning fluids promotes larger recirculation zones inside the feeding capillaries. The less viscous

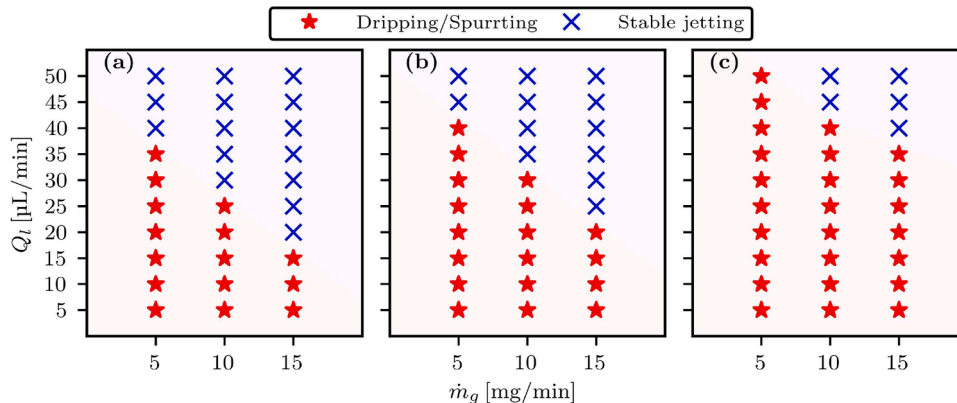


Fig. 13. Phase diagram of liquid jets with (a) shear-thinning, (b) Newtonian, and (c) shear-thickening rheology.

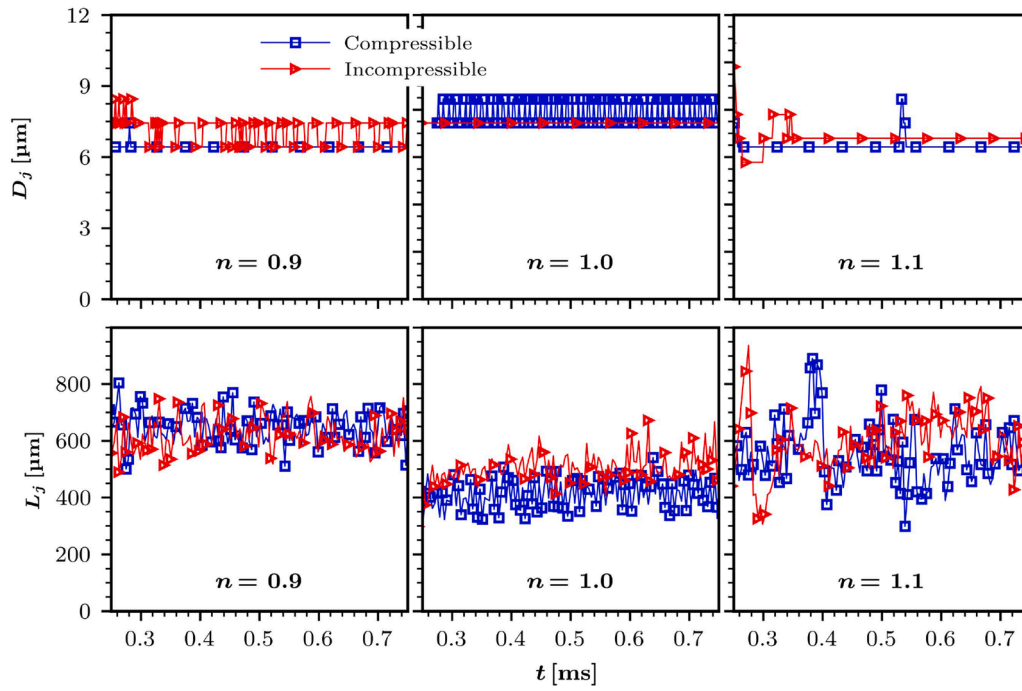


Fig. 14. Evolution of jet diameter (top) and jet length (bottom) for power law index of 0.9, 1.0, and 1.1, calculated with compressible and incompressible model.

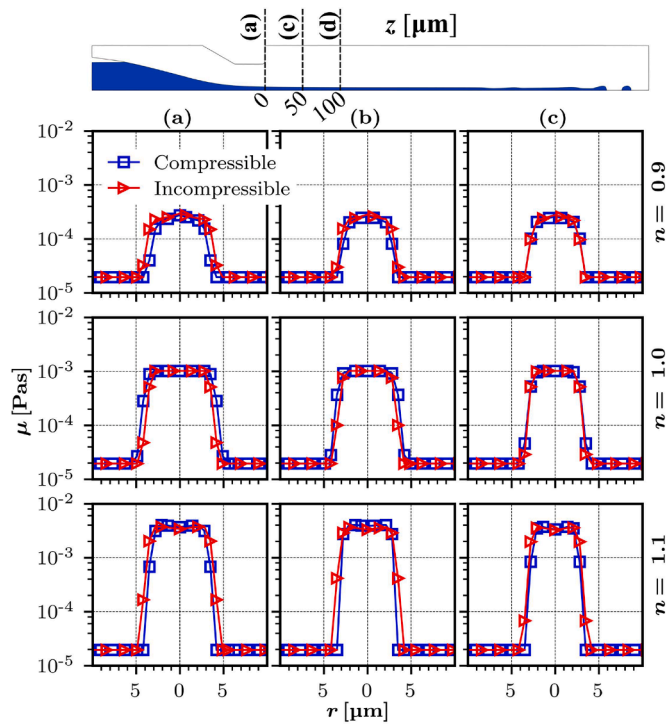


Fig. 15. Liquid viscosity as a function of the radius at three axial positions (0, 50, and 100 μm) for power law index of 0.9, 1.0, and 1.1, calculated with compressible and incompressible model.

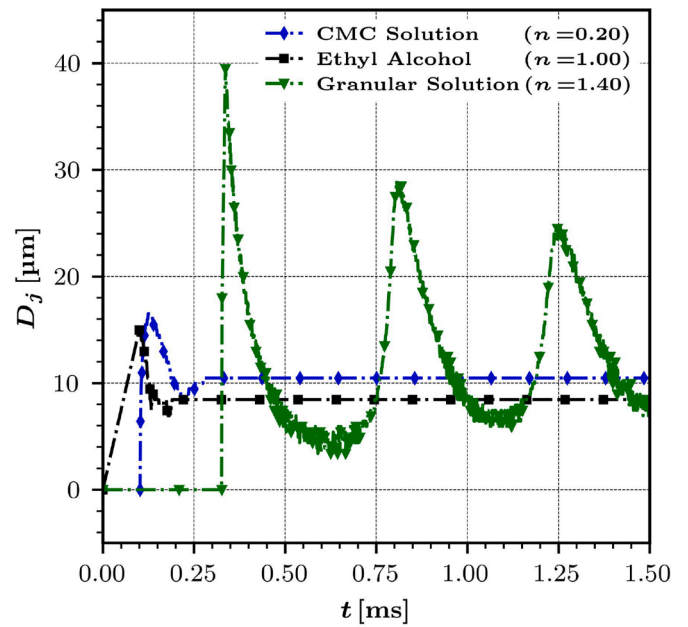


Fig. 16. Evolution of the jet diameter for Newtonian (ethyl alcohol), shear-thinning (CMC solution), and shear-thickening (granular solution) fluids.

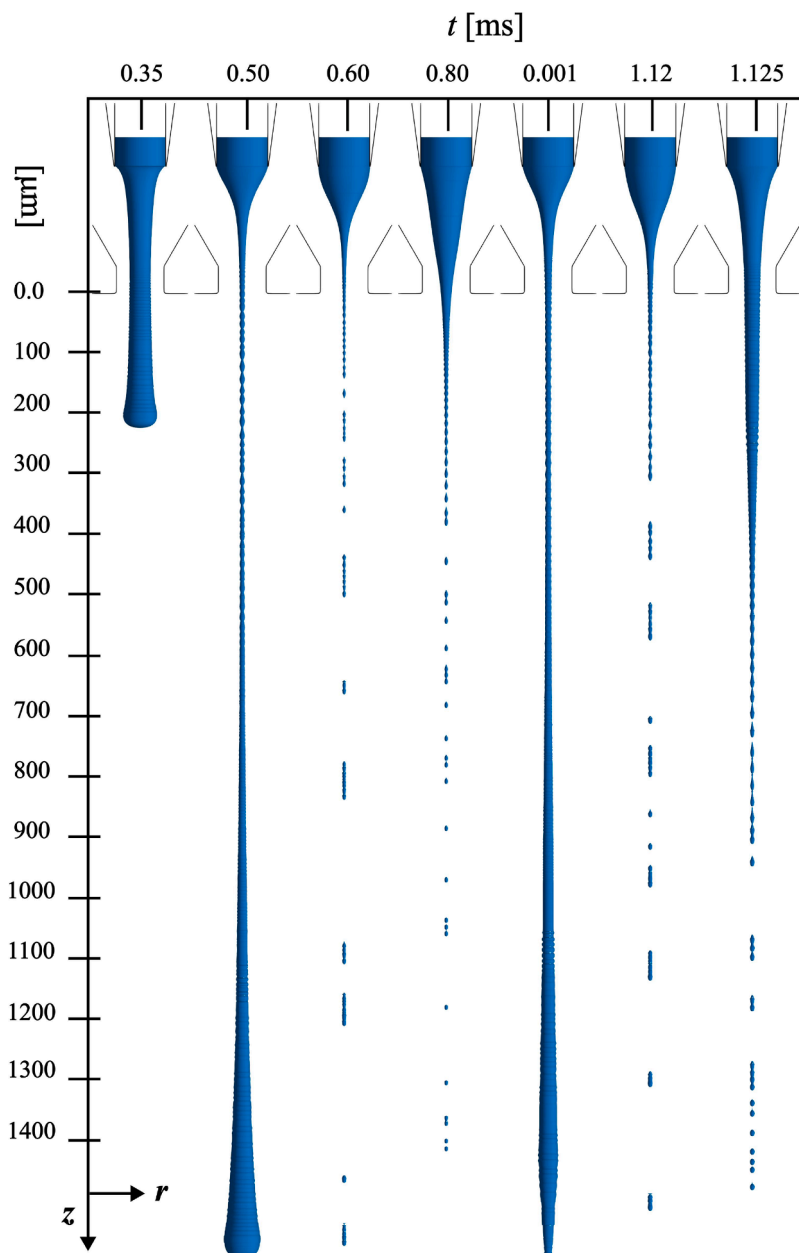


Fig. 17. Temporal evolution of a jet with shear-thickening (granular solution) fluid.

jets issuing from the nozzle are thus thicker, longer, and slower. On the other hand, the shear-thickening fluids are more resistant to the recirculation tendency. The more effective momentum transfer between the gas and liquid phases thus ensures a thinner and faster jet. The thinner jets are found to be more influenced by the surface tension forces, thus breaking earlier and resulting in shorter jets. The shear stresses in the vicinity of the jet are analysed and found to be higher for shear-thickening liquids. For the given gas and liquid flow rates, the jetting process ceased to occur at a power-law index higher than 1.10. A higher force from co-flowing gas is thus needed to stabilize the jets with highly viscous fluids. Finally, a set of thinning, Newtonian and thickening fluids are investigated and compared. The shear-thinning fluids provide more stable and thicker jets, while in shear-thickening fluids, a periodic generation of thick and thin jets is formed.

The present investigation provides a new dimension in the design of sample delivery systems for serial crystallography. The present study

shows how modifying the rheology of the sample-carrying fluid alters the jet's behaviour, which could be beneficial in some XFEL experiments. For example, a plug-like flow of non-Newtonian jets, with minimal shear stress over their cross-section, might be beneficial for embedded protein crystals in SFX experiments.

Declaration of Competing Interest

The authors declare that they have no known competing financial interests or personal relationships that could have appeared to influence the work reported in this paper.

Data availability

Data will be made available on request.

Acknowledgment

The funding for this research is provided by the Center for Free-Electron Laser Science (CFEL) under the project: Innovative methods for imaging with the use of X-ray free-electron laser (XFEL) and synchrotron sources: simulation of gas-focused micro-jets, and Slovenian Grant Agency (ARRS) within Program Group P2-0162 and Project J2-4477. This work is also partly supported by the Cluster of Excellence "CUI: Advanced Imaging of Matter" of the Deutsche Forschungsgemeinschaft (DFG)-EXC 2056-project ID390715994.

References

- Ahrens, J., Geveci, B., Law, C., 2005. ParaView: an end-user tool for large-data visualization. *Visualization Handbook*. Elsevier, New York, pp. 717–731. <https://doi.org/10.1016/B978-012387582-2/50038-1>.
- Aliseda, A., Hopfinger, E.J., Lasheras, J.C., Kremer, D.M., Berchielli, A., Connolly, E.K., 2008. Atomization of viscous and non-Newtonian liquids by a coaxial, high-speed gas jet: experiments and droplet size modeling. *Int. J. Multiph. Flow* 34, 161–175. <https://doi.org/10.1016/j.ijmultiphaseflow.2007.09.003>.
- Baek, G., Kim, C., 2011. Rheological properties of Carbolol containing nanoparticles. *J. Rheol.* 55, 313–330. <https://doi.org/10.1122/1.3538092>.
- Belsák, G., Bajt, S., Šarler, B., 2021. Numerical study of the micro-jet formation in double flow focusing nozzle geometry using different water-alcohol solutions. *Materials* 14, 3614. <https://doi.org/10.3390/ma14133614>.
- Bergmann, U., Pellegrini, C., Sauter, N., Ourmazd, A., Ekeberg, T., Spence, J., Zwart, P., DePonte, D., Weierstall, U., Orville, A., 2017. *X-Ray Free Electron Lasers: Applications in Materials, Chemistry and Biology*. Royal Society of Chemistry, United Kingdom.
- Beyerlein, K.R., Adriano, L., Heymann, M., Kirian, R., Knoška, J., Wilde, F., Chapman, H. N., Bajt, S., 2015. Ceramic micro-injection molded nozzles for serial femtosecond crystallography sample delivery. *Rev. Sci. Instrum.* 86, 125104. <https://doi.org/10.1063/1.4936843>.
- Blanco-Trejo, S., Herrada, M.A., Gañán-Calvo, A.M., Rubio, A., Cabezas, M.G., Montanero, J.M., 2020. Whipping in gaseous flow focusing. *Int. J. Multiph. Flow* 130, 103367. <https://doi.org/10.1016/j.ijmultiphaseflow.2020.103367>.
- Brackbill, J.U., Kothe, D.B., Zemach, C., 1992. A continuum method for modeling surface tension. *J. Comput. Phys.* 100, 335–354. [https://doi.org/10.1016/0021-9991\(92\)90240-Y](https://doi.org/10.1016/0021-9991(92)90240-Y).
- Byron, B.R., Carreau, P.J., 1968. A nonlinear viscoelastic model for polymer solutions and melts—I. *Chem. Eng. Sci.* 23, 427–434. [https://doi.org/10.1016/0009-2509\(68\)87018-6](https://doi.org/10.1016/0009-2509(68)87018-6).
- Carreau, P.J., 1972. Rheological equations from molecular network theories. *Trans. Soc. Rheol.* 16, 99–127. <https://doi.org/10.1122/1.549276>.
- Casson, N., 1959. *A Flow Equation for Pigment-Oil Suspensions of the Printing Ink Type, Rheology of Disperse Systems*. Pergamon Press, Oxford.
- Chapman, H.N., Fromme, P., Barty, A., White, T.A., Kirian, R.A., Aquila, A., Hunter, M.S., Schulz, J., DePonte, D.P., Weierstall, U., Doak, R.B., Maia, F.R.N.C., Martin, A.V., Schlichting, I., Lomb, L., Coppola, N., Shoeman, R.L., Epp, S.W., Hartmann, R., Rolles, D., Rudenko, A., Foucar, L., Kimmel, N., Weidenspointner, G., Holl, P., Liang, M., Barthelmeß, M., Caleman, C., Boutet, S., Bogan, M.J., Krzywinski, J., Bostedt, C., Bajt, S., Gumprecht, L., Rudek, B., Erk, B., Schmidt, C., Hömke, A., Reich, C., Pietschner, D., Strüder, L., Hauser, G., Gorke, H., Ullrich, J., Herrmann, S., Schaller, G., Schopper, F., Soltau, H., Kühnel, K.U., Messerschmidt, M., Bozek, J.D., Hau-Riege, S.P., Frank, M., Hampton, C.Y., Sierra, R.G., Starodub, D., Williams, G.J., Hajdu, J., Timneanu, N., Seibert, M.M., Andreasson, J., Røckner, A., Jönsson, O., Svenda, M., Stern, S., Nass, K., Andritschke, R., Schröter, C.D., Krasniqi, F., Bott, M., Schmidt, K.E., Wang, X., Grotjohann, I., Holton, J.M., Barends, T.R.M., Neutze, R., Marchesini, S., Fromme, R., Schorb, S., Rupp, D., Adolph, M., Gorkhaver, T., Andersson, I., Hirsemann, H., Potdevin, G., Graafsma, H., Nilsson, B., Spence, J.C.H., 2011. Femtosecond X-ray protein nanocrystallography. *Nature* 470, 73–77. <https://doi.org/10.1038/nature09750>.
- Chen, Q., Li, J., Song, Y., Christopher, D.M., Li, X., 2020. Modeling of newtonian droplet formation in power-law non-newtonian fluids in a flow-focusing device. *Heat Mass Transf.* 56, 2711–2723. <https://doi.org/10.1007/s00231-020-02899-6>.
- Cheng, R.K., 2020. Towards an optimal sample delivery method for serial crystallography at XFEL. *Crystals* 10, 215. <https://doi.org/10.1016/j.cry.2020.10.015>.
- Courant, R., Friedrichs, K., Lewy, H., 1967. On the partial difference equations of mathematical physics. *IBM J. Res. Dev.* 11, 215–234. <https://doi.org/10.1147/rd.112.0215>.
- Cross, M.M., 1965. Rheology of non-Newtonian fluids: a new flow equation for pseudoplastic systems. *J. Colloid Sci.* 20, 417–437. [https://doi.org/10.1016/0095-8522\(65\)90022-X](https://doi.org/10.1016/0095-8522(65)90022-X).
- Cruz-Mazo, F., Wiedorn, M.O., Herrada, M.A., Bajt, S., Chapman, H.N., Gañán-Calvo, A. M., 2019. Aerodynamically stabilized Taylor cone jets. *Phys. Rev. E* 100, 031101. <https://doi.org/10.1103/PhysRevE.100.031101>.
- Dean, J.A., 1990. *Lange's Handbook of Chemistry*. McGraw-Hill, New York.
- DePonte, D.P., Weierstall, U., Schmidt, K., Warner, J., Starodub, D., Spence, J.C.H., Doak, R.B., 2008. Gas dynamic virtual nozzle for generation of microscopic droplet streams. *J. Phys. D Appl. Phys.* 41, 195505. <https://doi.org/10.1088/0022-3727/41/19/195505>.
- Derzsi, L., Kasprzyk, M., Plog, J.P., Garstecki, P., 2013. Flow focusing with viscoelastic liquids. *Phys. Fluids* 25, 092001. <https://doi.org/10.1063/1.4817995>.
- Dessimoz, A.L., Cavin, L., Renken, A., Kiwi-Minsker, L., 2008. Liquid-liquid two-phase flow patterns and mass transfer characteristics in rectangular glass microreactors. *Chem. Eng. Sci.* 63, 4035–4044. <https://doi.org/10.1016/j.ces.2008.05.005>.
- Dupin, M.M., Halliday, L., Care, C.M., 2006. Simulation of a microfluidic flow-focusing device. *Phys. Rev. E* 73, 055701. <https://doi.org/10.1103/PhysRevE.73.055701>.
- Echelmeier, A., Sonker, M., Ros, A., 2019. Microfluidic sample delivery for serial crystallography using XFELs. *Anal. Bioanal. Chem.* 411, 6535–6547. <https://doi.org/10.1007/s00216-019-01977-x>.
- Edmond, K.V., Schofield, A.B., Marquez, M., Rothstein, J.P., Dinsmore, A.D., 2006. Stable jets of viscoelastic fluids and self-assembled cylindrical capsules by hydrodynamic focusing. *Langmuir* 22, 9052–9056. <https://doi.org/10.1021/la0614987>.
- Ertl, M., Weigand, B., Fritsching, U., 2016. Direct numerical simulations of shear-thinning liquid jets and droplets. *Process-Spray*. Springer International Publishing, Cham, pp. 647–678. https://doi.org/10.1007/978-3-319-32370-1_17.
- Ferziger, J.H., Perić, M., 2002. *Computational Methods for Fluid Dynamics*, 3rd ed. Springer, Berlin.
- Finehout, E., Tian, W.C., 2009. *Microfluidics for Biological Applications*. Springer US, Boston, MA.
- Fontana, F., Ferreira, M.P.A., Correia, A., Hirvonen, J., Santos, H.A., 2016. Microfluidics as a cutting-edge technique for drug delivery applications. *J. Drug Deliv. Sci. Technol.* 34, 76–87. <https://doi.org/10.1016/j.jddst.2016.01.010>.
- Gañán-Calvo, A.M., 1998. Generation of steady liquid microthreads and micron-sized monodisperse sprays in gas streams. *Phys. Rev. Lett.* 80, 285–288. <https://doi.org/10.1103/PhysRevLett.80.285>.
- Greenshields, C.J., 2022. *OpenFOAM User Guide*. The OpenFOAM Foundation, London.
- Grünbein, M.L., Kovacs, G.N., 2019. Sample delivery for serial crystallography at free-electron lasers and synchrotrons. *Acta Crystallogr. D Struct. Biol.* 75, 178–191. <https://doi.org/10.1107/S205979831801567X>.
- Günther, A., Jensen, K.F., 2006. Multiphase microfluidics: from flow characteristics to chemical and materials synthesis. *Lab Chip* 6, 1487–1503.
- Hejzian, M., Darmanin, C., Balaur, E., Abbey, B., 2020. Mixing and jetting analysis using continuous flow microfluidic sample delivery devices. *RSC Adv.* 10, 15694–15701. <https://doi.org/10.1039/D0RA00232A>.
- Herrada, M.A., Gañán-Calvo, A.M., Ojeda-Monge, A., Bluth, B., Riesco-Chueca, P., 2008. Liquid flow focused by a gas: jetting, dripping, and recirculation. *Phys. Rev. E* 78, 036323. <https://doi.org/10.1103/PhysRevE.78.036323>.
- Hirt, C.W., Nichols, B.D., 1981. Volume of fluid (VOF) method for the dynamics of free boundaries. *J. Comput. Phys.* 39, 201–225. [https://doi.org/10.1016/0021-9991\(81\)90145-5](https://doi.org/10.1016/0021-9991(81)90145-5).
- Hofmann, E., Krüger, K., Haynl, C., Scheibel, T., Trebbin, M., Förster, S., 2018. Microfluidic nozzle device for ultrafine fiber solution blow spinning with precise diameter control. *Lab Chip* 18, 2225–2234. <https://doi.org/10.1039/C8LC00304A>.
- Huerre, P., Monkewitz, P.A., 1990. Local and global instability in spatially developing flows. *Annu. Rev. Fluid Mech.* 22, 473–537. <https://doi.org/10.1146/annurev.fl.22.010190.002353>.
- Hunter, J.D., 2007. Matplotlib: a 2D graphics environment. *Comput. Sci. Eng.* 9, 90–95. <https://doi.org/10.1109/MCSE.2007.55>.
- Knoška, J., Adriano, L., Awel, S., Beyerlein, K.R., Yefanov, O., Oberthuer, D., Peña Murillo, G.E., Roth, N., Sarrou, I., Villanueva-Perez, P., Wiedorn, M.O., Wilde, F., Bajt, S., Chapman, H.N., Heymann, M., 2020. Ultracompact 3D microfluidics for time-resolved structural biology. *Nat. Commun.* 11, 657. <https://doi.org/10.1038/s41467-020-14434-6>.
- Kumari, P., Atta, A., 2022. Insights into the dynamics of non-Newtonian droplet formation in a T-junction microchannel. *Phys. Fluids* 34, 062001. <https://doi.org/10.1063/5.0092012>.
- Lee, T.Y., Choi, T.M., Shim, T.S., Frijns, R.A.M., Kim, S.H., 2016. Microfluidic production of multiple emulsions and functional microcapsules. *Lab Chip* 16, 3415–3440. <https://doi.org/10.1039/C6LC00809G>.
- LeVeque, R.J., 2002. *Finite Volume Methods for Hyperbolic Problems*. Cambridge University Press, Cambridge.
- Li, F., Gañán-Calvo, A.M., López-Herrera, J.M., Yin, X.Y., Yin, X.Z., 2013. Absolute and convective instability of a charged viscoelastic liquid jet. *J. Non Newton Fluid Mech.* 196, 58–69. <https://doi.org/10.1016/j.jnnfm.2013.01.003>.
- Lin, C.X., Ko, S.Y., 1995. Effects of temperature and concentration on the steady shear properties of aqueous solutions of carbopol and CMC. *Int. Commun. Heat Mass Transf.* 22, 157–166. [https://doi.org/10.1016/0735-1933\(95\)00001-1](https://doi.org/10.1016/0735-1933(95)00001-1).
- Martiel, I., Müller-Werkmeister, H.M., Cohen, A.E., 2019. Strategies for sample delivery for femtosecond crystallography. *Struct. Biol.* D75, 160–177. <https://doi.org/10.1107/S2059798318017953>.
- Moukalled, F., Mangani, L., Darwish, M., 2016. *The Finite Volume Method in Computational Fluid Dynamics: An Advanced Introduction with OpenFOAM and Matlab*. Springer International Publishing.
- Navi, M., Abbasi, N., Jeyhani, M., Gnyawali, V., Tsai, S.S.H., 2018. Microfluidic diamagnetic water-in-water droplets: a biocompatible cell encapsulation and manipulation platform. *Lab Chip* 18, 3361–3370. <https://doi.org/10.1039/C8LC00867A>.
- Nazari, R., Ansari, A., Herrmann, M., Adrian, R.J., Kirian, R.A., 2023. Numerical and experimental investigation of gas flow field variations in three-dimensional printed gas-dynamic virtual nozzles. *Front. Mech. Eng.* 8, 958963. <https://doi.org/10.3389/fmeh.2022.958963>.
- Negri, M., Ciekij, H.K., Schleichriem, S., 2013. Spray behavior of non-Newtonian fluids: correlation between rheological measurements and droplets/threads formation. *Progress in Propulsion Physics*. Presented at the Progress in Propulsion Physics. EDP

- Sciences, St. Petersburg, Russian, pp. 271–290. <https://doi.org/10.1051/eucass/201304271>.
- Nelson, G., Kirian, R.A., Weierstall, U., Zatsepin, N.A., Faragó, T., Baumbach, T., Wilde, F., Niesler, F.B.P., Zimmer, B., Ishigami, I., Hikita, M., Bajt, S., Yeh, S.R., Rousseau, D.L., Chapman, H.N., Spence, J.C.H., Heymann, M., 2016. Three-dimensional-printed gas dynamic virtual nozzles for x-ray laser sample delivery. *Opt. Express* 24, 11515. <https://doi.org/10.1364/OE.24.011515>.
- Neutze, R., Wouts, R., van der Spoel, D., Weckert, E., Hajdu, J., 2000. Potential for biomolecular imaging with femtosecond X-ray pulses. *Nature* 406, 752–757. <https://doi.org/10.1038/35021099>.
- Nilghaz, A., Mousavi, S.M., Li, M., Tian, J., Cao, R., Wang, X., 2021. Paper based microfluidics for food safety and quality analysis. *Trends Food Sci. Technol.* 118, 273–284.
- Oberthuer, D., Knoška, J., Wiedorn, M.O., Beyerlein, K.R., Bushnell, D.A., Kovaleva, E.G., Heymann, M., Gumprecht, L., Kirian, R.A., Barty, A., Mariani, V., Tolstikova, A., Adriano, L., Awel, S., Barthelmess, M., Dörner, K., Xavier, P.L., Yefanov, O., James, D.R., Nelson, G., Wang, D., Calvey, G., Chen, Y., Schmidt, A., Szczechpek, M., Frielingsdorf, S., Lenz, O., Snell, E., Robinson, P.J., Šarler, B., Belšak, G., Maček, M., Wilde, F., Aquila, A., Boutet, S., Liang, M., Hunter, M.S., Scheerer, P., Lipscomb, J.D., Weierstall, U., Kornberg, R.D., Spence, J.C.H., Pollack, L., Chapman, H.N., Bajt, S., 2017. Double-flow focused liquid injector for efficient serial femtosecond crystallography. *Sci. Rep.* 7, 44628. <https://doi.org/10.1038/srep44628>.
- Ponce-Torres, A., Montanero, J.M., Vega, E.J., Gañán-Calvo, A.M., 2016. The production of viscoelastic capillary jets with gaseous flow focusing. *J. Non Newton. Fluid Mech.* 229, 8–15. <https://doi.org/10.1016/j.jnnfm.2016.01.004>.
- Qiu, D., Silva, L., Tonkovich, A.L., Arora, R., 2010. Micro-droplet formation in non-Newtonian fluid in a microchannel. *Microfluid Nanofluid* 8, 531–548. <https://doi.org/10.1007/s10404-009-0487-5>.
- Rayleigh, L., 1879. On the capillary phenomena of jets. *Proc. R. Soc. Lond.* 29, 71–97. <https://doi.org/10.1098/rsp1.1879.0015>.
- Reiner, M., 1926. Ueber die Strömung einer elastischen Flüssigkeit durch eine Kapillare. *Kolloid-Zeitschrift* 39, 80–87. <https://doi.org/10.1007/BF01425357>.
- Rostami, B., Morini, G.L., 2019. Experimental characterization of a micro cross-junction as generator of Newtonian and non-Newtonian droplets in silicone oil flow at low capillary numbers. *Exp. Therm. Fluid Sci.* 103, 191–200. <https://doi.org/10.1016/j.expthermflusc.2019.01.008>.
- Rubio, A., Galindo-Rosales, F.J., Vega, E.J., Montanero, J.M., Cabezas, M.G., 2022a. Viscoelastic transition in transonic flow focusing. *Phys. Rev. Fluids* 7, 074201. <https://doi.org/10.1103/PhysRevFluids.7.074201>.
- Rubio, A., Vega, E.J., Gañán-Calvo, A.M., Montanero, J.M., 2022b. Unexpected stability of micrometer weakly viscoelastic jets. *Phys. Fluids* 34, 062014. <https://doi.org/10.1063/5.0091095>.
- Rubio, M., Rubio, A., Cabezas, M.G., Herrada, M.A., Gañán-Calvo, A.M., Montanero, J.M., 2021. Transonic flow focusing: stability analysis and jet diameter. *Int. J. Multiph. Flow* 142, 103720. <https://doi.org/10.1016/j.ijmultiphaseflow.2021.103720>.
- Šarler, B., Zahoor, R., Bajt, S., 2021. Alternative geometric arrangements of the nozzle outlet orifice for liquid micro-jet focusing. *Int. J. Gas dynamic virtual nozzles. Materials* 14. <https://doi.org/10.3390/ma14061572>.
- Shi, Y., Tang, G.H., 2015. Lattice Boltzmann simulation of droplet formation in non-Newtonian fluids. *Commun. Comput. Phys.* 17, 1056–1072. <https://doi.org/10.4208/cicp.2014.m333>.
- Sontti, S.G., Atta, A., 2017. CFD analysis of microfluidic droplet formation in non-Newtonian liquid. *Chem. Eng. J.* 330, 245–261. <https://doi.org/10.1016/j.cej.2017.07.097>.
- Stone, H.A., Stroock, A.D., Ajdari, A., 2004. Engineering flows in small devices: microfluidics toward a Lab-on-a-Chip. *Annu. Rev. Fluid Mech.* 36, 381–411. <https://doi.org/10.1146/annurev.fluid.36.050802.122124>.
- Sun, J., Warden, A.R., Ding, X., 2019. Recent advances in microfluidics for drug screening. *Biomicrofluidics* 13, 061503.
- van Leer, B., 1979. Towards the ultimate conservative difference scheme. V. A second-order sequel to Godunov's method. *J. Comput. Phys.* 32, 101–136. [https://doi.org/10.1016/0021-9991\(79\)90145-1](https://doi.org/10.1016/0021-9991(79)90145-1).
- Vega, E.J., Montanero, J.M., Herrada, M.A., Gañán-Calvo, A.M., 2010. Global and local instability of flow focusing: the influence of the geometry. *Phys. Fluids* 22, 1–10. <https://doi.org/10.1063/1.3450321>.
- Versteeg, H.K., Malalasekera, W., 2007. *Fluid, An Introduction to Computational Dynamics: The Finite Volume Method*, 2nd Ed. Pearson Education Limited, Harlow.
- Weierstall, U., 2014. Liquid sample delivery techniques for serial femtosecond crystallography. *Phil. Trans. R. Soc. B* 369, 20130337. <https://doi.org/10.1098/rstb.2013.0337>.
- Weller H.G., 2008. A new approach to VOF-based interface capturing methods for incompressible and compressible flow. Technical Report 13.
- Wiedorn, M.O., Awel, S., Morgan, A.J., Ayer, K., Gevorkov, Y., Fleckenstein, H., Roth, N., Adriano, L., Bean, R., Beyerlein, K.R., Chen, J., Coe, J., Cruz-Mazo, F., Ekeberg, T., Graceffa, R., Heymann, M., Horke, D.A., Knoška, J., Mariani, V., Nazari, R., Oberthür, D., Samanta, A.K., Sierra, R.G., Stan, C.A., Yefanov, O., Rompotis, D., Correa, J., Erk, B., Treusch, R., Schulz, J., Hogue, B.G., Gañán-Calvo, A.M., Fromme, P., Küpper, J., Rode, A.V., Bajt, S., Kirian, R.A., Chapman, H.N., 2018. Rapid sample delivery for megahertz serial crystallography at X-ray FELs. *IUCr* 5, 574–584. <https://doi.org/10.1107/S2052252518008369>.
- Zahoor, R., Bajt, S., Šarler, B., 2021a. A numerical investigation of micro-jet characteristics in different pressure environments. *Int. J. Hydromechatronics* 4, 368–383. <https://doi.org/10.1504/IJHM.2021.120618>.
- Zahoor, R., Bajt, S., Šarler, B., 2018a. Influence of gas dynamic virtual nozzle geometry on micro-jet characteristics. *Int. J. Multiph. Flow* 104, 152–165. <https://doi.org/10.1016/j.ijmultiphaseflow.2018.03.003>.
- Zahoor, R., Bajt, S., Šarler, B., 2018b. Numerical investigation on influence of focusing gas type on liquid micro-jet characteristics. *IJHM* 1, 222. <https://doi.org/10.1504/IJHM.2018.092732>.
- Zahoor, R., Belšak, G., Bajt, S., Šarler, B., 2018c. Simulation of liquid micro-jet in free expanding high speed co-flowing gas streams. *Microfluid Nanofluidics* 22, 87. <https://doi.org/10.1007/s10404-018-2110-0>.
- Zahoor, R., Knoška, J., Bajt, S., Šarler, B., 2021b. Experimental and numerical investigation of gas-focused liquid micro-jet velocity. *Int. J. Multiph. Flow* 135, 103530. <https://doi.org/10.1016/j.ijmultiphaseflow.2020.103530>.
- Zahoor, R., Regvar, R., Bajt, S., Šarler, B., 2020. A numerical study on the influence of liquid properties on gas-focused micro-jets. *Prog. Comput. Fluid Dyn. Int. J.* 20, 71–83. <https://doi.org/10.1504/PCFD.2020.106407>.
- Zhang, F., Zirwes, T., Müller, T., Wächter, S., Jakobs, T., Habisreuther, P., Zarzalis, N., Trimis, D., Kolb, T., 2020. Effect of elevated pressure on air-assisted primary atomization of coaxial liquid jets: basic research for entrained flow gasification. *Renew. Sustain. Energy Rev.* 134, 110411. <https://doi.org/10.1016/j.rser.2020.110411>.
- Zhao, F., Zhang, B., Yan, E., Sun, B., Wang, Z., He, J., Yin, D., 2019. A guide to sample delivery systems for serial crystallography. *FEBS J.* 286, 4402–4417. <https://doi.org/10.1111/febs.15099>.
- Zupan, B., Peña-Murillo, G.E., Zahoor, R., Gregorc, J., Šarler, B., Knoška, J., Gañán-Calvo, A.M., Chapman, H.N., Bajt, S., 2023. An experimental study of liquid micro-jets produced with a gas dynamic virtual nozzle under the influence of an electric field. *Front. Mol. Biosci.* 10, 1006733. <https://doi.org/10.3389/fmolb.2023.1006733>.